Funneling and spin-orbit coupling in transition metal dichalcogenide nanotubes and wrinkles

M. Daqiqshirazi and T. Brumme*

Chair of Theoretical Chemistry, Faculty of Chemistry and Food Chemistry, TU Dresden, Bergstraße 66c, 01069 Dresden, Germany

(Received 19 July 2023; revised 8 September 2023; accepted 11 September 2023; published 13 October 2023)

Strain engineering provides a powerful means to tune the properties of two-dimensional materials. Accordingly, numerous studies have investigated the effect of bi- and uniaxial strain. Yet, the strain fields in many systems such as nanotubes and nanoscale wrinkles are intrinsically inhomogeneous and the consequences of this symmetry breaking are much less studied. Understanding how this affects the electronic properties is crucial, especially since wrinkling is a powerful method to apply strain to two-dimensional materials in a controlled manner. In this paper, we employ density functional theory to understand the correlation between the atomic and the electronic structure in nanoscale wrinkles and nanotubes of the prototypical transition metal dichalcogenide WSe_2. Our research shows that the symmetry breaking in these structures leads to strong Rashba-like splitting of the bands at the Γ point and they thus may be utilized in future tunable spintronic devices. The inhomogeneous strain reduces the band gap and leads to a localization of the band edges in the highest-curvature region, thus funneling excitons there. Moreover, we show how wrinkles can be modeled as nanotubes with the same curvature and when this comparison breaks down and further inhomogeneities have to be taken into account.

DOI: 10.1103/PhysRevB.108.155304

I. INTRODUCTION

Two-dimensional (2D) materials have been the focus of a myriad of research in the last decade due to their fascinating properties. After the successful synthesis of graphene [1], other materials such as hexagonal boron nitride (h-BN) [2], transition metal dichalcogenides (TMDCs) [3–6], and black phosphorous [7] joined the class of 2D materials quite quickly. Many researchers investigated the intriguing properties of this new class of materials, such as their extraordinary strength and high deformation before rupture, high mobility, and ease of property alteration [8–14]. 2D materials have proved to be useful for many applications, such as nanoelectronics, spintronics, and catalysis [15–18].

Still, researchers are trying to expand the applicability of these materials by methods such as alloying [19], introduction of defects [20], creation of van der Waals heterostructures, or by applying external pressure and fields [21,22]. Another method offering a reversible and nondestructive route to modulate the properties of 2D materials is strain engineering [23–30]. Uniaxial and biaxial strains have been studied extensively [31,32] and there are standard techniques which can already be used during the synthesization of 2D materials [12]. Often the application of in-plane stress will lead to the formation of wrinkles and there are established methods to produce these wrinkles [33], which can even be used to determine the mechanical properties of the layered material [34–36]. Furthermore, the changes of the electronic structure in these wrinkles leads to funneling, i.e., a preferential emission of light from a certain spatial position along the wrinkle [28,30,37–40]. However, the local strain in such samples is far from being homogeneous and the comparison with calculations of homogeneously strained systems might be misleading. Understanding this (local) inhomogeneous strain in 2D materials requires further research due to the vast opportunities for future applications such as polarized single photon emitters [41,42] and flexible optoelectronics [23].

In order to understand the influence of the inhomogeneous strain in 2D systems, one can study idealized model systems which have a similar strain state, but are easier to control from an experimental point of view or need less approximations in the respective theoretical description. Nanotubes (NTs) are structures where strain fields can play an important role [43,44] and even though those are not strictly inhomogeneous, since the strain can be defined by a constant curvature, they represent such a simple model system which is different from the uni- or biaxially strained 2D layers and closer to the wrinkled systems in experiments.

The investigation of the electronic properties of inhomogeneously strained materials requires methods such as density functional theory (DFT) or density functional based tight binding (DFTB), which can be computationally demanding for large systems. Fortunately, for NTs, researchers have developed a method to reduce the size of the curved systems: cyclic DFT [45–47] employs the helical boundary condition in nanotubes in order to reduce the cost of the calculation and this method was successfully used to determine the bending modulus of various 2D systems. It is important to investigate the similarities and differences of NTs and wrinkles because this understanding is crucial, as in larger wrinkles (or other systems where the variation of strain is due to a variation of the local curvature) it is computationally impossible to entirely model the system. NTs could then be used to further simplify the calculation by the use of cyclic DFT.

*thomas.brumme@tu-dresden.de

The sheer size of inhomogeneously strained structures causes many theoretical investigations to neglect relativistic effects beyond scalar-relativistic limits in order to enhance computational speed. Including spin-orbit coupling (SOC) in systems with heavy elements (such as TMDCs) is, however, very important in order to understand the many fascinating physical effects occurring in 2D materials, such as the Hall effect at room temperature [48], the Rashba effect [49,50], and spin-valley coupling [51].

The Rashba effect, i.e., the emergence of spin splitting in momentum direction [49,52], occurs due to inversion symmetry breaking in the presence of SOC. Such splitting was initially observed in zinc blends, wurtzite, and in systems under an external electric field. Another type of system in which this splitting is observed is Janus-type 2D materials due to the resulting internal electric field perpendicular to the structure. Yet, the internal electric field and the subsequent splitting are quite small $\alpha \approx \mathcal{O}$ (10 meV Å). Cheng *et al.* [53] studied such polar TMDCs (WSSe as an example), proving their stability, and recommended them to be used for Datta-Das spin field effect transistors. This behavior can be even more interesting if the splitting manifests adjustability without the need of an external electric field. Yao *et al.* [54] utilized biaxial strain to manipulate the Rashba splitting in Janus heterostructures and concluded that the change of orbital overlaps increases the splitting. Since many symmetries including inversion symmetry are broken in curved systems such as NTs and wrinkles, one could also imagine the emergence of similar phenomena especially since such a curvature-induced SOC has already been shown for carbon NTs [55,56].

Having mentioned the importance of inhomogeneous strain in 2D structures, in this paper, we theoretically investigate WSe_2 in the form of NTs and wrinkles. We concentrate on these systems specifically since we also want to estimate if and when NTs can be used to model large-scale wrinkles in order to ease the computational load using helical boundary conditions. The similarities between NTs and wrinkles are expounded and strain associated phenomena in the band structures are described. We explore NTs and wrinkles in a large range with an *ab initio* method including SOC effects, which provides electronic insight about these materials for better future applications.

II. RESULTS AND DISCUSSION

In the following, we will investigate how inhomogeneous strain affects wrinkles and NTs of monolayer WSe_2—a prototypical example of the TMDCs. In order to compare wrinkles and NTs, the initial wrinkled structure was created with a circular profile as shown in Fig. 1, with a wavelength to amplitude ratio of $\lambda/A = 4$ and using NTs as input. We will discuss the deformation energy and changes in the band dispersion and we will explain the origin of funneling in nanoscale wrinkles as well as a Rashba-like splitting that occurs in curved TMDC structures. We will further explain in detail the similarities of the electronic structure of NTs and wrinkles.

A. Deformation energy/band gaps

The relaxation of the initial structure is very different for NTs and wrinkles. While the former only change the diameter [cf. Figs. 1(b) and 1(c)], the latter relax into structures which no longer resemble the initial nanotubelike profile [Figs. 1(e) and 1(f)], especially in the region close to the middle plane of the unit cell (inflection point). In this region, the wrinkled structure resembles a flat monolayer and is thus under less local strain in comparison to the corresponding nanotube. However, the peak of the wrinkles deforms stronger, leading to areas with higher curvature. The curvature in NTs, on the other hand, is constant since they always remain circular [Fig. 1(c)]. In order to allow for a better comparison between NTs and wrinkles, we will introduce two measures—the average and the minimum radius of curvature, R_{ave} and R_{min}—by fitting a spline to the positions of the tungsten atoms and calculating its curvature. The comparison of the deformation energies E_{def} as a function of the average radius of curvature in Fig. 2 shows that there is a small difference between NTs and wrinkles for the smaller systems (i.e., with larger average curvature), while the difference between armchair and zigzag is negligible. The deformation energy E_{def} has been calculated as follows:

$$E_{\text{def}} = \frac{E_{\text{sys}}}{N_{\text{u.c.}}} - E_{\text{mono}}, \tag{1}$$

where E_{sys} is the energy of the wrinkle/nanotube, $N_{\text{u.c.}}$ is the number of formula units, and E_{mono} is the energy of the flat monolayer. This indicates that the local relaxation at the inflection point of the wrinkles and the corresponding increasing curvature at the maxima can be understood as a redistribution of the strain which leads to a total energy gain. Figure 2 furthermore shows that this energy gain (per formula unit) becomes very small for $R_{\text{ave}} \gtrsim 25$ Å.

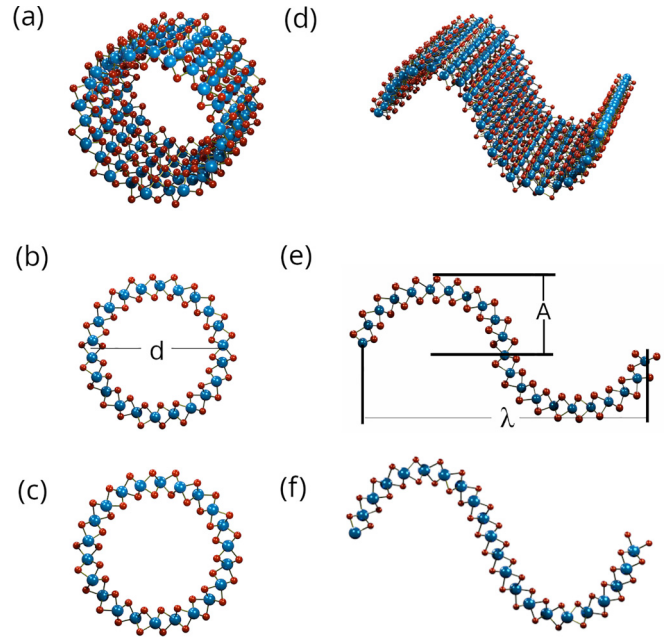

FIG. 1. WSe_2 structures investigated in this study. (a),(b) Nanotube 3D and side view; (d),(e) wrinkle 3D and side view (periodic boundary condition on back and front); (c),(f) side view of the relaxed nanotube and wrinkle, respectively. The structural parameters such as the nanotube diameter "d" and the amplitude or wavelength of the wrinkle, "A" or λ, are indicated in (b) and (e). Wrinkles with an initially elliptical profile ($\lambda = 4A$) relax into a structure with smoother areas between peaks and valleys.

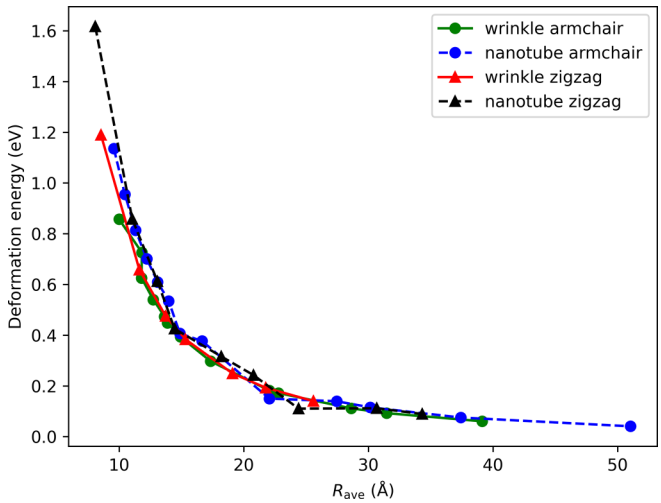

FIG. 2. Variation of the deformation energy with increasing average radius of curvature, R_{ave}, i.e., with increasing wavelength and diameter for wrinkles and nanotubes, respectively.

Interestingly, the profile of the relaxed wrinkles differs from the sinusoidal wave which is assumed in continuum mechanics and which follows from the harmonic approximation. The deviation from the sinusoidal shape is more prominent for shorter wavelengths and vanishes for wrinkles with larger wavelength, which are more similar to monolayers. In fact, the long-range behavior is expected and can already be predicted by analyzing the average curvature of differently wrinkled curves (see the "Curvature analysis" section in the Supplemental Material (SM) for more details [57]). In brief, for $\lambda/A \gtrapprox 3.5$, the profile tends to be sinusoidal, while for smaller λ/A, an elliptical or circular profile is preferred. This deviation from the harmonic solution is important for analyzing the strain fields using electron microscopy images for which one requires an assumption about the shape of the wrinkle (cf. Refs. [58,59]). Our structures with $\lambda \approx 4A$ after relaxation are, in fact, better fitted by two sine functions, with one having an almost three times larger wavelength.

Such wrinkle profiles, having periodically wrinkled areas with peaks and valleys, have already been observed in wrinkling experiments on polymeric substrate [22,35]. Yet, in other wrinkling experiments [60], single wrinkles with only peaks connected with areas of lower strain have been found. In order to keep the discussions in this paper general, we focus on fully relaxed wrinkles which correspond to the expected relaxed freestanding wrinkle profile. The investigation of substrate-induced effects is an interesting topic which is, however, beyond the current investigation.

The relaxation in the wrinkles leads to differences in the electronic structure compared to the nanotubelike structures used for the initial geometry. Yet, the comparison of the band dispersion for NTs and wrinkles with approximately the same average curvature (especially for large wavelength or diameter) also reveals similarities, especially for the conduction and valence bands (CB and VB). Figure 3 shows the band structures for a (24,24) nanotube ($d = 44$ Å) and the corresponding wrinkle ($\lambda = 88$ Å). Both the valence-band maximum (VBM) and conduction-band minimum (CBM) show large contributions from tungsten atoms (cf. Fig. S3 in

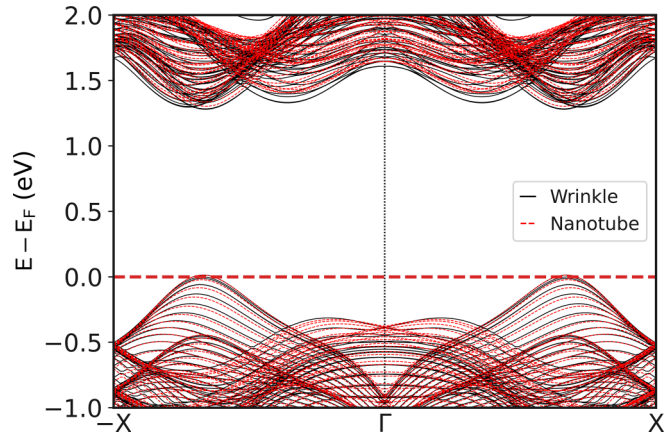

FIG. 3. Comparison of the band structures for the (24,24) nanotube and the corresponding wrinkle. The smallest direct band gap is the high-symmetry K point of the monolayer which is mapped to the $\Gamma - X$ line (cf. element-projected band structures in the SM [57], Fig. S3, and the "Brillouin zone of wrinkles/nanotubes and spin texture" section).

the SM [57] for the monolayer in the rectangular unit cell), indicating that those are the high-symmetry K points of the primitive unit cell which are mapped to the $\Gamma - X$ line (more details about the backfolding can be found in the SM [57], "Brillouin zone of wrinkles/NTs and spin texture" section). Not only is the global band gap E_{gap} comparable for this specific example, but also the dispersion of the first few VBs and CBs and, accordingly, the derived physical quantities such as mobility and conductivity. This is a promising outcome as it suggests that for global variables of large-scale wrinkles, a similar nanotube can be used to reduce the computational cost. In Fig. 4, we compare the direct band gap as a function of the average curvature for all investigated systems.

The global direct band gap of most wrinkles is slightly smaller than those of the NTs with similar average curvature and, in both systems, the band gap approaches the value of the monolayer, $E_{gap}^{ml} \approx 1.34$ eV, for small average curvature,

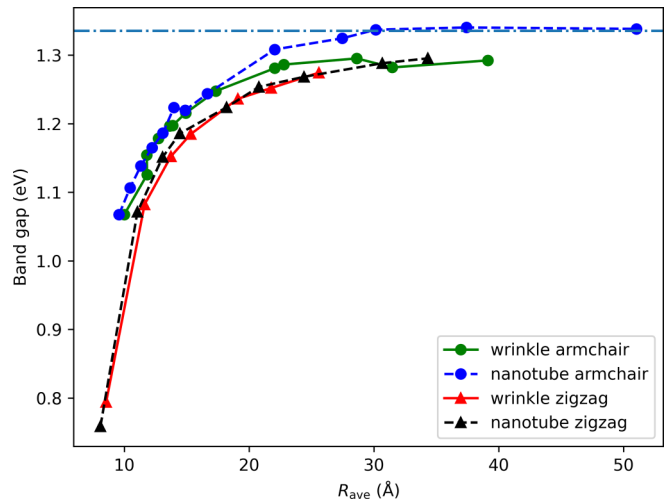

FIG. 4. Variation of the global direct band gap E_{gap} due to the strain field formed in wrinkles and nanotubes of WSe_2. The dash-dotted line indicates the direct band gap of the flat monolayer.

i.e., large radius of curvature—please note that the calculated band gap for the monolayer can vary depending on the settings [61]. Thus, NTs can possibly be used to model the global band gap changes in large wrinkles (or similar systems under inhomogeneous strain) if the average curvature of the wrinkles is taken into account. It is worthwhile to reemphasize that the *ab initio* modeling of inhomogeneous strain in wrinkles is computationally very demanding due to the symmetry breaking, the presence of many heavy atoms, and spin-orbit coupling, and that this similarity can be utilized to simplify the theoretical modeling. One can then subsequently utilize helical boundary conditions to further reduce the computational cost. However, there are also some differences for the bands close to the VBM/CBM—in wrinkles, we find more bands with similar dispersion but small differences in the maximum/minimum energy and this can explain the funneling found in wrinkled systems, as explained in the following.

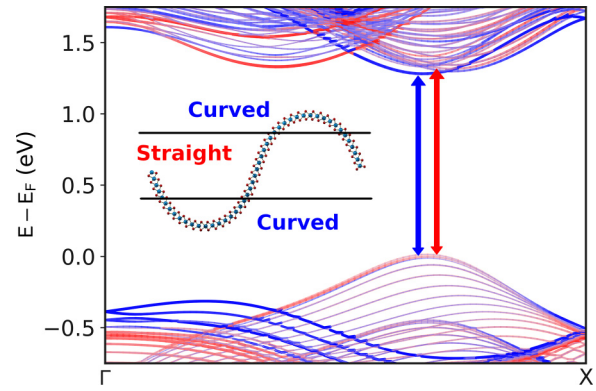

FIG. 5. Contribution of curved and straight sections of the (24,24) wrinkle to its band structure; the smallest local band gaps from each region are also indicated by arrows. The inset depicts the region division.

B. Funneling

Funneling is the phenomenon of absorption and emission of light from different spatial positions along the wrinkle. The directional guiding of the excitons can be achieved by a spatial modification of, e.g., the dielectric screening [62] or the band gap of the material due to external strain [37]. This phenomenon attracted the attention of numerous scientists and was subject to much research [28,30,37–39,63]. It has, for example, been shown that the photovoltaic behavior of 2D materials [64] and light-emitting diodes [65] can significantly be enhanced. Furthermore, it was proposed that highly directional exciton transport promises not only compelling advantages for exciton-based applications, but could also be interesting to reach truly 1D regimes to study the quantum transport phenomena of correlated many-body states [63]. From the experimental point of view, photoluminescence microscopy is routinely used to study these systems, although it can be quite challenging at the nanoscale [38]; other techniques such as time-resolved transient absorption microscopy [66] are possible too, but also need additional input from theory to interpret the results. However, in conjunction with theoretical estimates of the band structure changes due to external strain [38,67,68] or different stacking regions [67,69], a quantitative description of experimentally observed shifts of excitonic peaks is possible.

In order to understand the difference between all the bands close to the VBM and CBM and relate this to experimental observations, we projected the band structure on different atoms along the wrinkle. Figure 5 shows that the VBM is spread all over the wrinkle, while the VB-1 and VB-2 (the two bands below the VB) close to the VBM are more localized in the straight and the curved region, respectively. The CBM, on the other hand, is localized at the top of the wrinkle in the regions with large local strain, while the higher CB also shows contributions from the straight regions. Since the different minima of the CBs have a larger difference in energy than the VBs, the lowest band gap is found in the regions with large local curvature. Figures S14a and S14b in the SM [57] show the variation of the local density of states (LDOS) along the (24,24) wrinkle close to VBM and CBM, respectively, and confirm that the energy levels close to the band gap are more localized close to the peaks and valleys of the wrinkle. Yet, since the band extrema also have small differences in the momentum direction which complicate the situation, further studies using, e.g., the Bethe-Salpeter equation to describe the excitonic states are needed, which are—at the moment—however, only possible for the smallest systems of our study [40]. Nevertheless, as shown previously, the changes of the local band gap give a very good estimate of the shifts of the excitonic peaks [38,67,68].

Another important effect which will influence the dynamics of excitons is the internal electric fields, which are induced by the curvature [70]. In order to estimate the local electric field which results from the local curvature, we use the dipoles as calculated with the Hirshfeld partitioning scheme [71]. Figure 6 shows the magnitude and direction of the tungsten dipoles for the (24,24) wrinkle. One can clearly see that the dipoles at the peaks and valleys of the wrinkle are larger—due to this inhomogeneity, there will be an effective electric field which could be another force driving the excitons to the

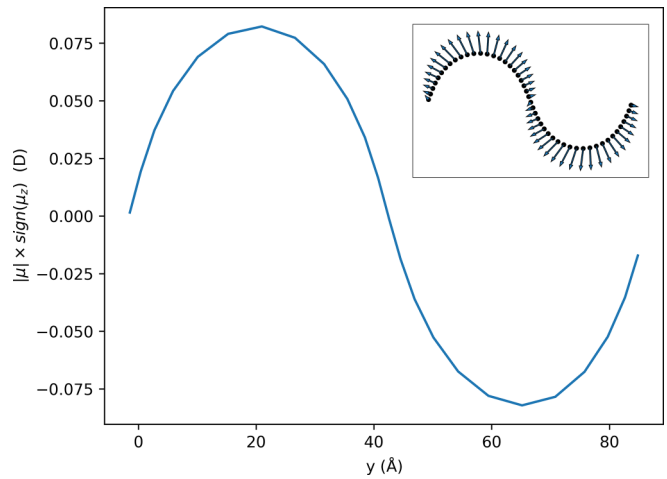

FIG. 6. Magnitude of the Hirshfeld dipole vectors [71] of the tungsten atoms along the (24,24) wrinkle. In order to better visualize the position along the wrinkle, the magnitude has the same sign as the z component, μ_z. The inset sketches the rotation of the dipole vectors along the wrinkle (black balls are the W positions).

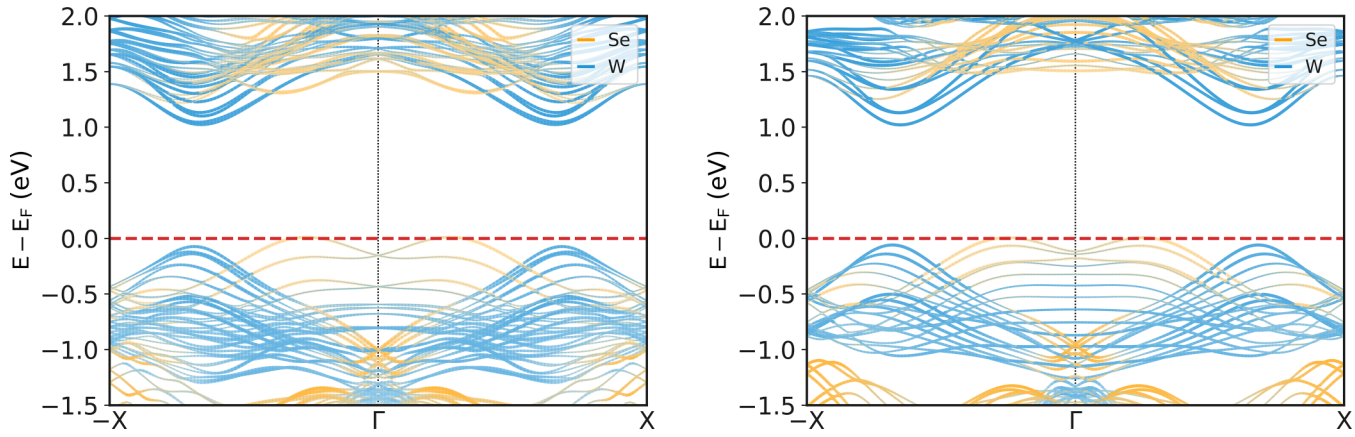

FIG. 7. Band structure of the (11,11) wrinkle (left) and nanotube (right). The Rashba-like splitting in the momentum direction is clearly visible for the VB in the vicinity of the Γ point and is—for this system with a small λ/A ratio—even above the former VBM at the K point.

regions with higher curvature. This inhomogeneity can also be seen in the contour plot of the total electrostatic potential; see Fig. S13 in the SM [57]. Yet, in experiments, the screening by a substrate might be important as well and we will leave this fascinating topic for future work since this is beyond the current investigation.

Most interestingly, the internal electric field due to the dipoles leads to a Rashba-like SOC splitting, as can be seen in Fig. 3 and in Fig. S15 in the SM [57] for the CB states crossing at the Γ point.

C. SOC splitting

The splitting of the bands close to the Γ point resembles the Rashba spin-orbit splitting found in quantum wells or Janus-type TMDCs [72,73]. By comparing band structures with and without SOC (shown in the SM [57], Fig. S16), we can directly see the effect of SOC on the band dispersion. We observed this Rashba-like splitting (i.e., splitting of the band energies in momentum direction [49]) in all investigated systems and furthermore found in very small NTs an apparent avoided crossing of the SOC-split states, which might be either due to the interaction between atoms of opposite sides or an artifact due to possible strain-induced changes of the hexagonal symmetry (cf. Fig. 7 and Fig. S7 in the SM [57]).

The Rashba splitting in nanoscale wrinkles and NTs occurs due to the symmetry breaking caused by the inhomogeneous strain field and the resulting electric dipoles perpendicular to the wrinkle and nanotube. Hence, in the presence of spin-orbit coupling, two degenerate spin bands split into two separate bands in the momentum direction. These SOC-split states are mainly localized at the top (i.e., highest curvature part) of the wrinkle (cf. Fig. 5).

Figure 7 depicts the band structure of the armchair (11,11) wrinkle and nanotube, also highlighting the changes with increasing curvature if compared to Fig. 3—the splitting not only increases in the momentum direction, but the Rashba-split states also move up in energy such that they eventually become the VBM (see, also, Figs. S17–S20 in the SM [57]). One main difference of the wrinkle with respect to the nanotube is the larger splitting between the uppermost VBs and the lower bands, which might be due to the higher curvature at the top of the wrinkles and the more diverse local strain state in the wrinkles.

Another important difference can be found in the spin texture of the highest valence bands and lowest conduction bands, as shown in the "Brillouin zone of wrinkles/NTs and spin texture" section in the SM [57]. While the NTs always show twofold degenerate bands coming from the K and K′ point of the 2D material, the degeneracy is slightly lifted in the wrinkle, probably due to the different strain states along one period of the wrinkle. In fact, a slight asymmetry is also visible in the contour plot of the total electrostatic potential shown in Fig. S9 of the SM [57]. This also leads to a different spin texture (compared to the NT) in which the VB of the wrinkle does not automatically have the opposite spin expectation value of the band just below (VB-1). The largest contribution of $\langle\sigma_i\rangle$ for the Rashba-split states close to Γ is always coming from $\langle\sigma_y\rangle$ and $\langle\sigma_z\rangle$, i.e., the directions perpendicular to $\mathbf{k}$. Furthermore, Figs. S5 and S7 in the SM [57] show that for the wrinkle, the lowest CB has the opposite spin polarization of the VB at the K point (the extrema closer to the X point); the inhomogeneous strain is not large enough to change the pattern, which is also observed in the monolayer [74].

Figure 8 depicts the expectation value $\langle\sigma_z\rangle$ for the four highest valence bands of the (11,11) wrinkle. Note that close to Γ, only two bands are visible since the bands are doubly degenerate due to the folding to the 1D Brillouin zone. We thus show the average expectation value of the two degenerate states, $(\langle\sigma_z\rangle_1 + \langle\sigma_z\rangle_2)/2$. The expectation values $\langle\sigma_x\rangle$ and $\langle\sigma_y\rangle$ are either zero or the two degenerate states have opposite signs. A complete discussion about the individual spin states can be found in the SM [57], Figs. S5–S8.

In order to examine the strength of the Rashba-like splitting, the Rashba coupling parameter [75] α_R has been calculated for the armchair systems using

$$\alpha_R = \frac{2E_R}{k_R}, \tag{2}$$

where E_R and k_R are the Rashba energy and the shift of the bands in the momentum direction, respectively. Unfortunately, the different back folding of the bands in the zigzag structures leads to the primitive unit cell's K point being

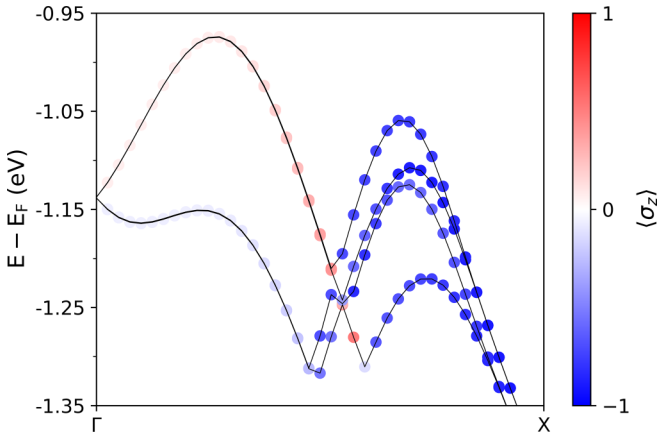

FIG. 8. The expectation value $\langle\sigma_z\rangle$ for the (11,11) wrinkle is shown by the colored dots for the four highest valence bands. Note that only two bands are visible since the bands are doubly degenerate due to the folding to the 1D Brillouin zone.

mapped to Γ, thus obscuring the SOC-split states. This prevents an easy and correct fitting of the Rashba model to the band structure, even if the band structures in the SM [57] clearly show the same splitting.

The Rashba coupling parameter shown in Fig. 9 decreases as the wrinkle wavelength or nanotube diameter increases. This trend can be explained by the decreasing strain difference between the outer and the inner chalcogen layer and the corresponding smaller induced electric field. It is also evident that the band gap and band dispersion of large NTs and wrinkles are converging to the corresponding flat monolayer (cf. Figs. S3 and S19 in the SM [57]). Furthermore, the Rashba coupling parameter is only comparable between wrinkles and NTs if it is shown with respect to the minimum radius of curvature, R_{min}, i.e., the highest curvature. This is once more due to the wrinkles having higher curvature at their peaks. The Rashba coupling parameter in our structures is relatively high and almost half the size of elemental surfaces [76], and one order of magnitude larger than in Janus-type TMDCs [53,77].

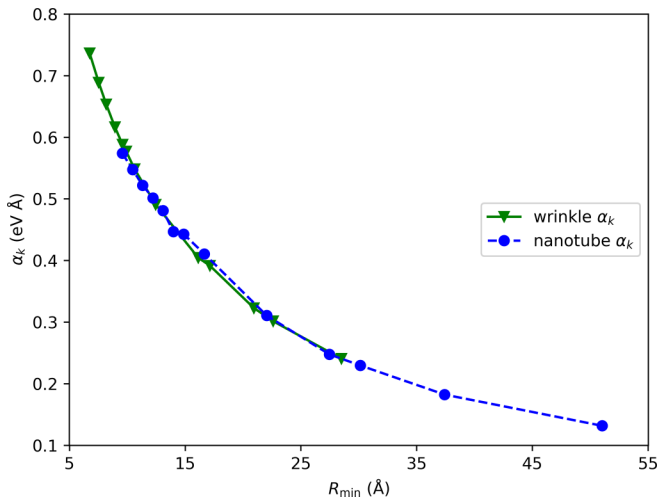

FIG. 9. The Rashba coupling parameter in armchair WSe_2 nanotubes and wrinkles. The splitting reduces as the R_{min} increases, i.e., as the local strain due to the curvature decreases.

Furthermore, the coupling parameter in wrinkles/NTs with small R_{min} can also be comparable to the one found in heterostructures, including BiSb [78], even if one probably needs to include higher-order terms to properly describe the large splitting [79]. It should be noted that the largest splittings are those that are easiest to reach experimentally since the bands move above the monolayer VBM at K. This is also a possibility for tuning the electronic structure and the SOC-induced splitting for the application in spintronic devices: using (mono)layers of TMDCs deposited on elastic substrates which can be used to induce different wrinkle morphologies as shown in, e.g., Refs. [80,81].

It should be noted, however, that the exact shape of the wrinkle can be different from our research, e.g., due to substrate effects; the conclusions in the above sections still hold as they are due to strain effects and the subsequent symmetry breaking. Yet, slight quantitative differences are expected and require further investigation. We expect that nanotubes can still be used to model the curvature effects in wrinkled systems and that the variation of the local band gap leads to exciton funneling. Furthermore, the interaction with substrates and additional external fields might lead to even higher Rashba-like splittings.

III. CONCLUSION

We investigated NTs and 2D wrinkles of WSe_2 theoretically and analyzed the influence of the induced inhomogeneous strain on their electronic properties, but the following conclusions should generally apply to all TMDCs. We found that the inhomogeneous strain causes symmetry breaking in these structures, which leads to a Rashba-like splitting of the valence band at Γ. Therefore, these structures—particularly the smaller wavelengths—could be promising candidates for spintronic applications. In fact, spin-polarized scanning tunneling microscope (STM) using an additional graphene layer as an electrode [82,83] should be able to measure the Rashba-like splitting of the VBM. We believe that this is a general feature of wrinkled 2D TMDCs due to the nonuniform strain and our study will thus pave the way for the employment of a wide range of materials in spintronic devices. This bears witness to the important role of SOC in the physics of 2D TMDC nanoscale wrinkles and NTs. Moreover, wrinkling should be regarded as a method to introduce out-of-plane dipoles in the 2D system which might be useful in other contexts. Investigations of bilayers and heterostructures made of dichalcogenides could even result in the appearance of more fascinating phenomena.

Furthermore, nanoscale TMDC wrinkles do not follow a sine wave profile as suggested by continuum mechanics and which has been widely utilized in strain analysis. The profiles in our study are basically composed of a superposition of two sine waves. Thus, the curvature varies more smoothly in the profile's maxima and minima. This suggests that the classical formulation of such structures conceals important physical properties and so conclusions based upon it might be misleading, e.g., in the calculation of strain fields from the surface topology in nanoscale wrinkles. Moreover, we attribute the funneling of excitons to the localization of states in different spatial locations due to the presence of the inhomogeneous

strain. Yet, more advanced calculations are needed to evaluate the influence of, e.g., the induced dipoles or substrate, and an additional investigation of the wrinkled samples via STM [82,83] could furthermore help one to better understand the band alignment.

Additionally, we demonstrated that NTs can be used to approximate the wrinkles for a reduction of computational costs. Nonetheless, one needs to take care of the differences that exist.

IV. METHODS

NTs and wrinkles of a monolayer of WSe_2 having two edge types, i.e., armchair and zigzag, were investigated using an all-electron method based on DFT as implemented in FHI-AIMS code [84]. We utilized the Perdew-Burke-Ernzerhof (PBE) exchange-correlation functional [85] together with the Tkatchenko-Scheffler dispersion correction [86] and the non-self-consistent SOC implementation [87]. Additionally, no symmetry was imposed on any of the structures in these calculations. In order to compare wrinkles and NTs, the initial wrinkled structure was created with an elliptical profile, as shown in Fig. 1, with a wavelength to amplitude ratio of $\lambda/A = 4$ and using NTs as input. The unit cell was fixed only in the direction of the wrinkles with λ to retain the compression. All structures have been relaxed utilizing the Broyden-Fletcher-Godfarb-Shanno method to reach forces below 1 meV/Å. Subsequently, the Mulliken projected band structures with and without spin-orbit coupling were calculated. NTs are labeled with the rolling vector (m,n), and for wrinkles, a similar notation is used such that the (m,n) wrinkle is similar to the (m,n) nanotube.

The geometries as well as the band structures for all systems which have been investigated within this work were uploaded to the NOMAD repository; see Ref. [88].

ACKNOWLEDGMENTS

The authors would like to thank Professor T. Heine, Dr. A. Kuc, R. Kempt, and F. Arnold for fruitful discussions. This project was financially supported by the SFB 1415, Project ID No. 417590517. We would like to acknowledge the Center for Information Service and High Performance Computing [Zentrum für Informationsdienste und Hochleistungsrechnen (ZIH)] at TU Dresden. The authors gratefully acknowledge the Gauss Centre for Supercomputing e.V. [89] for funding this project by providing computing time through the John von Neumann Institute for Computing (NIC) on the GCS Supercomputer JUWELS [90] at Jülich Supercomputing Centre (JSC).

There are no conflicts of interest to declare.

[1] K. S. Novoselov, A. K. Geim, S. V. Morozov, D. Jiang, Y. Zhang, S. V. Dubonos, I. V. Grigorieva, and A. A. Firsov, Electric field effect in atomically thin carbon films, Science **306**, 666 (2004).

[2] L. Song, L. Ci, H. Lu, P. B. Sorokin, C. Jin, J. Ni, A. G. Kvashnin, D. G. Kvashnin, J. Lou, B. I. Yakobson *et al.*, Large scale growth and characterization of atomic hexagonal boron nitride layers, Nano Lett. **10**, 3209 (2010).

[3] A. Ayari, E. Cobas, O. Ogundadegbe, and M. S. Fuhrer, Realization and electrical characterization of ultrathin crystals of layered transition-metal dichalcogenides, J. Appl. Phys. **101**, 014507 (2007).

[4] A. Kuc, N. Zibouche, and T. Heine, Influence of quantum confinement on the electronic structure of the transition metal sulfide TS_2, Phys. Rev. B **83**, 245213 (2011).

[5] T. Lorenz, M. Ghorbani-Asl, J.-O. Joswig, T. Heine, and G. Seifert, Is MoS_2 a robust material for 2D electronics? Nanotechnology **25**, 445201 (2014).

[6] H. Xu, J. Zhu, Q. Ma, J. Ma, H. Bai, L. Chen, and S. Mu, Two-dimensional MoS_2: Structural properties, synthesis methods, and regulation strategies toward oxygen reduction, Micromachines **12**, 240 (2021).

[7] A. H. Woomer, T. W. Farnsworth, J. Hu, R. A. Wells, C. L. Donley, and S. C. Warren, Phosphorene: Synthesis, scale-up, and quantitative optical spectroscopy, ACS Nano **9**, 8869 (2015).

[8] P. Miró, M. Audiffred, and T. Heine, An atlas of two-dimensional materials, Chem. Soc. Rev. **43**, 6537 (2014).

[9] M. Ghorbani-Asl, A. Kuc, P. Miro, and T. Heine, A single-material logical junction based on 2D crystal PdS_2, Adv. Mater. **28**, 853 (2016).

[10] D. Akinwande, C. J. Brennan, J. S. Bunch, P. Egberts, J. R. Felts, H. Gao, R. Huang, J.-S. Kim, T. Li, Y. Li *et al.*, A review on mechanics and mechanical properties of 2D materials graphene and beyond, Extreme Mech. Lett. **13**, 42 (2017).

[11] T. Brumme, M. Calandra, and F. Mauri, First-principles theory of field-effect doping in transition-metal dichalcogenides: Structural properties, electronic structure, Hall coefficient, and electrical conductivity, Phys. Rev. B **91**, 155436 (2015).

[12] Z. Dai, L. Liu, and Z. Zhang, Strain engineering of 2D materials: Issues and opportunities at the interface, Adv. Mater. **31**, 1805417 (2019).

[13] Y. K. Hong, N. Liu, D. Yin, S. Hong, D. H. Kim, S. Kim, W. Choi, and Y. Yoon, Recent progress in high-mobility thin-film transistors based on multilayer 2D materials, J. Phys. D **50**, 164001 (2017).

[14] A. Falin, M. Holwill, H. Lv, W. Gan, J. Cheng, R. Zhang, D. Qian, M. R. Barnett, E. J. Santos, K. S. Novoselov *et al.*, Mechanical properties of atomically thin tungsten dichalcogenides: WS_2, WSe_2, and WTe_2, ACS Nano **15**, 2600 (2021).

[15] E. C. Ahn, 2D materials for spintronic devices, npj 2D Mater. Appl. **4**, 17 (2020).

[16] Z. Lu, G. P. Neupane, G. Jia, H. Zhao, D. Qi, Y. Du, Y. Lu, and Z. Yin, 2D materials based on main group element compounds: Phases, synthesis, characterization, and applications, Adv. Funct. Mater. **30**, 2001127 (2020).

[17] Z. Li, N. H. Attanayake, J. L. Blackburn, and E. M. Miller, Carbon dioxide and nitrogen reduction reactions using 2D transition metal dichalcogenide (TMDC) and carbide/nitride (MXene) catalysts, Energy Environ. Sci. **14**, 6242 (2021).

[18] S. Anju and P. Mohanan, Biomedical applications of transition metal dichalcogenides (TMDCs), Synth. Met. **271**, 116610 (2020).

[19] Y.-C. Lin, R. Torsi, D. B. Geohegan, J. A. Robinson, and K. Xiao, Controllable thin-film approaches for doping and alloying transition metal dichalcogenides monolayers, Adv. Sci. **8**, 2004249 (2021).

[20] M. Ghorbani-Asl, S. Kretschmer, and A. V. Krasheninnikov, Two-dimensional materials under ion irradiation: From defect production to structure and property engineering, in *Defects in Two-Dimensional Materials*, Materials Today, edited by R. Addou and L. Colombo (Elsevier, Amsterdam, 2022), Chap. 9, pp. 259–301.

[21] Q. Ma, G. Ren, K. Xu, and J. Z. Ou, Tunable optical properties of 2D materials and their applications, Adv. Opt. Mater. **9**, 2001313 (2021).

[22] H. Daghigh Shirazi, Y. Dong, J. Niskanen, C. Fedele, A. Priimagi, V. P. Jokinen, and J. Vapaavuori, Multiscale hierarchical surface patterns by coupling optical patterning and thermal shrinkage, ACS Appl. Mater. Interfaces **13**, 15563 (2021).

[23] J. Du, H. Yu, B. Liu, M. Hong, Q. Liao, Z. Zhang, and Y. Zhang, Strain engineering in 2D material-based flexible optoelectronics, Small Methods **5**, 2000919 (2021).

[24] G. Plechinger, A. Castellanos-Gomez, M. Buscema, H. S. Van Der Zant, G. A. Steele, A. Kuc, T. Heine, C. Schueller, and T. Korn, Control of biaxial strain in single-layer molybdenite using local thermal expansion of the substrate, 2D Mater. **2**, 015006 (2015).

[25] M. Ghorbani-Asl, N. Zibouche, M. Wahiduzzaman, A. F. Oliveira, A. Kuc, and T. Heine, Electromechanics in MoS_2 and WS_2: Nanotubes vs. monolayers, Sci. Rep. **3**, 2961 (2013).

[26] M. Ghorbani-Asl, S. Borini, A. Kuc, and T. Heine, Strain-dependent modulation of conductivity in single-layer transition-metal dichalcogenides, Phys. Rev. B **87**, 235434 (2013).

[27] T. Heine, Transition metal chalcogenides: Ultrathin inorganic materials with tunable electronic properties, Acc. Chem. Res. **48**, 65 (2015).

[28] Z. Peng, X. Chen, Y. Fan, D. J. Srolovitz, and D. Lei, Strain engineering of 2D semiconductors and graphene: From strain fields to band-structure tuning and photonic applications, Light Sci. Appl. **9**, 190 (2020).

[29] H. Jiang, L. Zheng, Z. Liu, and X. Wang, Two-dimensional materials: From mechanical properties to flexible mechanical sensors, InfoMat **2**, 1077 (2020).

[30] C. Di Giorgio, E. Blundo, G. Pettinari, M. Felici, F. Bobba, and A. Polimeni, Mechanical, elastic, and adhesive properties of two-dimensional materials: From straining techniques to state-of-the-art local probe measurements, Adv. Mater. Interfaces **9**, 2102220 (2022).

[31] S. Haastrup, M. Strange, M. Pandey, T. Deilmann, P. S. Schmidt, N. F. Hinsche, M. N. Gjerding, D. Torelli, P. M. Larsen, A. C. Riis-Jensen *et al.*, The computational 2D materials database: High-throughput modeling and discovery of atomically thin crystals, 2D Mater. **5**, 042002 (2018).

[32] R. Roldán, A. Castellanos-Gomez, E. Cappelluti, and F. Guinea, Strain engineering in semiconducting two-dimensional crystals, J. Phys.: Condens. Matter **27**, 313201 (2015).

[33] G. Lee, M. Zarei, Q. Wei, Y. Zhu, and S. G. Lee, Surface wrinkling for flexible and stretchable sensors, Small **18**, 2203491 (2022).

[34] A. Schweikart and A. Fery, Controlled wrinkling as a novel method for the fabrication of patterned surfaces, Microchim. Acta **165**, 249 (2009).

[35] A. Knapp, L. J. Nebel, M. Nitschke, O. Sander, and A. Fery, Controlling line defects in wrinkling: A pathway towards hierarchical wrinkling structures, Soft Matter **17**, 5384 (2021).

[36] Y. Yu, C. Ng, T. A. König, and A. Fery, Tackling the scalability challenge in plasmonics by wrinkle-assisted colloidal self-assembly, Langmuir **35**, 8629 (2019).

[37] J. Lee, S. J. Yun, C. Seo, K. Cho, T. S. Kim, G. H. An, K. Kang, H. S. Lee, and J. Kim, Switchable, tunable, and directable exciton funneling in periodically wrinkled WS_2, Nano Lett. **21**, 43 (2021).

[38] Y. Koo, Y. Kim, S. H. Choi, H. Lee, J. Choi, D. Y. Lee, M. Kang, H. S. Lee, K. K. Kim, G. Lee *et al.*, Tip-induced nano-engineering of strain, band gap, and exciton funneling in 2D semiconductors, Adv. Mater. **33**, 2008234 (2021).

[39] J. Shao, F. Chen, W. Su, N. Kumar, Y. Zeng, L. Wu, and H.-W. Lu, Probing nanoscale exciton funneling at wrinkles of twisted bilayer MoS_2 using tip-enhanced photoluminescence microscopy, J. Phys. Chem. Lett. **13**, 3304 (2022).

[40] J. Jiang and R. Pachter, Analysis of localized excitons in strained monolayer WSe_2 by first principles calculations, Nanoscale **14**, 11378 (2022).

[41] K. Parto, S. I. Azzam, K. Banerjee, and G. Moody, Defect and strain engineering of monolayer WSe_2 enables site-controlled single-photon emission up to 150k, Nat. Commun. **12**, 3585 (2021).

[42] Q. Wang, J. Maisch, F. Tang, D. Zhao, S. Yang, R. Joos, S. L. Portalupi, P. Michler, and J. H. Smet, Highly polarized single photons from strain-induced quasi-1D localized excitons in WSe_2, Nano Lett. **21**, 7175 (2021).

[43] R. Tenne, L. Margulis, M. e. Genut, and G. Hodes, Polyhedral and cylindrical structures of tungsten disulphide, Nature (London) **360**, 444 (1992).

[44] S. S. Sinha, L. Yadgarov, S. B. Aliev, Y. Feldman, I. Pinkas, P. Chithaiah, S. Ghosh, A. Idelevich, A. Zak, and R. Tenne, MoS_2 and WS_2 nanotubes: Synthesis, structural elucidation, and optical characterization, J. Phys. Chem. C **125**, 6324 (2021).

[45] S. Ghosh, A. S. Banerjee, and P. Suryanarayana, Symmetry-adapted real-space density functional theory for cylindrical geometries: Application to large group-IV nanotubes, Phys. Rev. B **100**, 125143 (2019).

[46] N. K. Nepal, L. Yu, Q. Yan, and A. Ruzsinszky, First-principles study of mechanical and electronic properties of bent monolayer transition metal dichalcogenides, Phys. Rev. Mater. **3**, 073601 (2019).

[47] S. Kumar and P. Suryanarayana, Bending moduli for 44 select atomic monolayers from first principles, Nanotechnology **31**, 43LT01 (2020).

[48] C. Safeer, J. Ingla-Aynés, N. Ontoso, F. Herling, W. Yan, L. E. Hueso, and F. Casanova, Spin Hall effect in bilayer graphene combined with an insulator up to room temperature, Nano Lett. **20**, 4573 (2020).

[49] A. Manchon, H. C. Koo, J. Nitta, S. Frolov, and R. Duine, New perspectives for Rashba spin-orbit coupling, Nat. Mater. **14**, 871 (2015).

[50] N. Zibouche, A. Kuc, J. Musfeldt, and T. Heine, Transition-metal dichalcogenides for spintronic applications, Ann. Phys. **526**, 395 (2014).

[51] J. Klein, J. Wierzbowski, P. Soubelet, T. Brumme, L. Maschio, A. Kuc, K. Müller, A. V. Stier, and J. J. Finley, Electrical control of orbital and vibrational interlayer coupling in bi-and trilayer 2H-MoS_2, Phys. Rev. Mater. **6**, 024002 (2022).

[52] J. Chen, K. Wu, W. Hu, and J. Yang, Spin–orbit coupling in 2D semiconductors: A theoretical perspective, J. Phys. Chem. Lett. **12**, 12256 (2021).

[53] Y. Cheng, Z. Zhu, M. Tahir, and U. Schwingenschlögl, Spin-orbit–induced spin splittings in polar transition metal dichalcogenide monolayers, Europhys. Lett. **102**, 57001 (2013).

[54] Q.-F. Yao, J. Cai, W.-Y. Tong, S.-J. Gong, J.-Q. Wang, X. Wan, C.-G. Duan, and J. H. Chu, Manipulation of the large Rashba spin splitting in polar two-dimensional transition-metal dichalcogenides, Phys. Rev. B **95**, 165401 (2017).

[55] W. Izumida, K. Sato, and R. Saito, Spin-orbit interaction in single wall carbon nanotubes: Symmetry adapted tight-binding calculation and effective model analysis, J. Phys. Soc. Jpn. **78**, 074707 (2009).

[56] L. Chico, M. P. López-Sancho, and M. C. Muñoz, Curvature-induced anisotropic spin-orbit splitting in carbon nanotubes, Phys. Rev. B **79**, 235423 (2009).

[57] See Supplemental Material at http://link.aps.org/supplemental/10.1103/PhysRevB.108.155304 for a simple model for the curvature analysis, tables with the average/maximum curvature of all investigated systems, a band structure of the unstrained monolayer in the rectangular unit cell, a discussion of the Brillouin zones of wrinkles/nanotubes including the spin expectation values for the four lowest/highest conduction/valence bands for the (11,11) systems and a brief discussion of the spin texture, contour plots of the total electrostatic potential for the (10,10) nanotube/wrinkle, the local density of states of the VBM/CBM along the (11,11) wrinkle, additional comparisons of the band structures of wrinkles and nanotubes, band structures projected onto specific regions of the wrinkles, and band structures near the Fermi energy for all investigated systems and the additional references [91–93].

[58] L. Xie and Y. Oshima, Quantitative estimation of atom-scaled ripple structure using transmission electron microscopy images, Nanotechnology **32**, 185703 (2021).

[59] L. Xie and Y. Oshima, Nonlinear mechanical response of rippled MoS_2 nanosheets evaluated by in situ transmission electron microscopy, Appl. Surf. Sci., **597** 153708 (2022).

[60] J. Wang, M. Han, Q. Wang, Y. Ji, X. Zhang, R. Shi, Z. Wu, L. Zhang, A. Amini, L. Guo *et al.*, Strained epitaxy of monolayer transition metal dichalcogenides for wrinkle arrays, ACS Nano **15**, 6633 (2021).

[61] T. N. Tran, M. T. Dang, Q. H. Tran, T. T. Luong, and V. A. Dinh, Band valley modification under strain in monolayer WSe_2, AIP Adv. **12**, 115023 (2022).

[62] N. Peimyoo, H.-Y. Wu, J. Escolar, A. De Sanctis, G. Prando, F. Vollmer, F. Withers, A. C. Riis-Jensen, M. F. Craciun, K. S. Thygesen, and S. Russo, Engineering dielectric screening for potential-well arrays of excitons in 2D materials, ACS Appl. Mater. Interfaces **12**, 55134 (2020).

[63] F. Dirnberger, J. D. Ziegler, P. E. F. Junior, R. Bushati, T. Taniguchi, K. Watanabe, J. Fabian, D. Bougeard, A. Chernikov, and V. M. Menon, Quasi-1D exciton channels in strain-engineered 2D materials, Sci. Adv. **7**, eabj3066 (2021).

[64] M. G. Harats and K. I. Bolotin, Limits of funneling efficiency in nonuniformly strained 2D semiconductors, 2D Mater. **8**, 015010 (2021).

[65] Y. Jiang, J. Wei, and M. Yuan, Energy-funneling process in quasi-2D perovskite light-emitting diodes, J. Phys. Chem. Lett. **12**, 2593 (2021).

[66] L. Yuan, B. Zheng, J. Kunstmann, T. Brumme, A. B. Kuc, C. Ma, S. Deng, D. Blach, A. Pan, and L. Huang, Twist-angle-dependent interlayer exciton diffusion in WS_2-WSe_2 heterobilayers, Nat. Mater. **19**, 617 (2020).

[67] C. Cho, J. Wong, A. Taqieddin, S. Biswas, N. R. Aluru, S. Nam, and H. A. Atwater, Highly strain-tunable interlayer excitons in MoS_2/WSe_2 heterobilayers, Nano Lett. **21**, 3956 (2021).

[68] Y. Koo, H. Lee, T. Ivanova, A. Kefayati, V. Perebeinos, E. Khestanova, V. Kravtsov, and K.-D. Park, Dynamical control of interlayer excitons and trions in $WSe_2/Mo_{0.5}W_{0.5}Se_2$ heterobilayer via tunable near-field cavity, arXiv:2203.02136.

[69] L. Yuan, B. Zheng, Q. Zhao, R. Kempt, T. Brumme, A. B. Kuc, C. Ma, S. Deng, A. Pan, and L. Huang, Strong dipolar repulsion of one-dimensional interfacial excitons in monolayer lateral heterojunctions, ACS Nano **17**, 15379 (2023).

[70] W. Shi, Y. Guo, Z. Zhang, and W. Guo, Flexoelectricity in monolayer transition metal dichalcogenides, J. Phys. Chem. Lett. **9**, 6841 (2018).

[71] F. L. Hirshfeld, Bonded-atom fragments for describing molecular charge densities, Theor. Chim. Acta **44**, 129 (1977).

[72] Z. Gan, I. Paradisanos, A. Estrada-Real, J. Picker, E. Najafidehaghani, F. Davies, C. Neumann, C. Robert, P. Wiecha, K. Watanabe *et al.*, Chemical vapor deposition of high-optical-quality large-area monolayer Janus transition metal dichalcogenides, Adv. Mater. **34**, 2205226 (2022).

[73] G. Yin, D. Zhu, D. Lv, A. Hashemi, Z. Fei, F. Lin, A. V. Krasheninnikov, Z. Zhang, H.-P. Komsa, and C. Jin, Hydrogen-assisted post-growth substitution of tellurium into molybdenum disulfide monolayers with tunable compositions, Nanotechnology **29**, 145603 (2018).

[74] X.-X. Zhang, Y. You, Shu Yang Frank Zhao, and T. F. Heinz, Experimental evidence for dark excitons in monolayer WSe_2, Phys. Rev. Lett. **115**, 257403 (2015).

[75] A. Kuc and T. Heine, The electronic structure calculations of two-dimensional transition-metal dichalcogenides in the presence of external electric and magnetic fields, Chem. Soc. Rev. **44**, 2603 (2015).

[76] G. Bihlmayer, O. Rader, and R. Winkler, Focus on the Rashba effect, New J. Phys. **17**, 050202 (2015).

[77] W. Liu, X. Li, C. Zhang, and S. Yan, Janus *vxy* monolayers with tunable large Berry curvature, J. Semicond. **43**, 042501 (2022).

[78] S. Singh and A. H. Romero, Giant tunable Rashba spin splitting in a two-dimensional BiSb monolayer and in BiSb/AlN heterostructures, Phys. Rev. B **95**, 165444 (2017).

[79] S. Gupta and B. I. Yakobson, What dictates Rashba splitting in 2D van der Waals heterobilayers, J. Am. Chem. Soc. **143**, 3503 (2021).

[80] D. Giambastiani, C. Tommasi, F. Bianco, F. Fabbri, C. Coletti, A. Tredicucci, A. Pitanti, and S. Roddaro, Strain-engineered wrinkles on graphene using polymeric actuators, Phys. Rev. Appl. **18**, 024069 (2022).

[81] H.-Y. Lee, G.-Z. Lu, J.-L. Shen, H.-Y. Lin, and Y.-F. Chen, Wrinkled 2D hybrid heterostructures for stretchable and sensitive photodetectors, J. Mater. Chem. C **10**, 16370 (2022).

[82] Z. Qiu, M. Holwill, T. Olsen, P. Lyu, J. Li, H. Fang, H. Yang, M. Kashchenko, K. S. Novoselov, and J. Lu, Visualizing atomic structure and magnetism of 2D magnetic insulators via tunneling through graphene, Nat. Commun. **12**, 70 (2021).

[83] R. Nieken, A. Roche, F. Mahdikhanysarvejahany, T. Taniguchi, K. Watanabe, M. R. Koehler, D. G. Mandrus, J. Schaibley, and B. J. LeRoy, Direct STM measurements of *r*-type and *h*-type twisted $MoSe_2/WSe_2$, APL Mater. **10**, 031107 (2022).

[84] V. Blum, R. Gehrke, F. Hanke, P. Havu, V. Havu, X. Ren, K. Reuter, and M. Scheffler, *Ab initio* molecular simulations with numeric atom-centered orbitals, Comput. Phys. Commun. **180**, 2175 (2009).

[85] J. P. Perdew, K. Burke, and M. Ernzerhof, Generalized gradient approximation made simple, Phys. Rev. Lett. **77**, 3865 (1996).

[86] A. Tkatchenko and M. Scheffler, Accurate molecular Van Der Waals interactions from ground-state electron density and free-atom reference data, Phys. Rev. Lett. **102**, 073005 (2009).

[87] W. P. Huhn and V. Blum, One-hundred-three compound band-structure benchmark of post-self-consistent spin-orbit coupling treatments in density functional theory, Phys. Rev. Mater. **1**, 033803 (2017).

[88] M. Daqiqshiraz and T. Brumme, The geometries as well as the band structures for all systems can be found on the NOMAD repository (2022), doi:10.17172/NOMAD/2022.08.31-1.

[89] https://www.gauss-centre.eu/.

[90] D. Alvarez, Juwels cluster and booster: Exascale pathfinder with modular supercomputing architecture at Juelich supercomputing centre, J. Large Scale Res. Facil. **7**, A183 (2021).

[91] R. Saito, G. Dresselhaus, and M. S. Dresselhaus, *Physical Properties of Carbon Nanotubes* (Imperial College Press/World Scientific, Singapore, 1998).

[92] P. Giannozzi, S. Baroni, N. Bonini, M. Calandra, R. Car, C. Cavazzoni, D. Ceresoli, G. L. Chiarotti, M. Cococcioni, I. Dabo, A. D. Corso, S. de Gironcoli, S. Fabris, G. Fratesi, R. Gebauer, U. Gerstmann, C. Gougoussis, A. Kokalj, M. Lazzeri, L. Martin-Samos *et al.*, QUANTUM ESPRESSO: A modular and open-source software project for quantum simulations of materials, J. Phys.: Condens. Matter **21**, 395502 (2009).

[93] P. Giannozzi, O. Andreussi, T. Brumme, O. Bunau, M. B. Nardelli, M. Calandra, R. Car, C. Cavazzoni, D. Ceresoli, M. Cococcioni, N. Colonna, I. Carnimeo, A. D. Corso, S. de Gironcoli, P. Delugas, R. A. DiStasio Jr, A. Ferretti, A. Floris, G. Fratesi, G. Fugallo *et al.*, Advanced capabilities for materials modelling with QUANTUM ESPRESSO, J. Phys.: Condens. Matter **29**, 465901 (2017).